JBC RESEARCH ARTICLE

Importance of RNA length for *in vitro* encapsidation by the nucleoprotein of human respiratory syncytial virus

Received for publication, April 23, 2022, and in revised form, July 21, 2022 Published, Papers in Press, August 3, 2022,
https://doi.org/10.1016/j.jbc.2022.102337

Lorène Gonnin[1], Charles-Adrien Richard[1], Irina Gutsche[2], Didier Chevret[1], Joris Troussier[3], Jean-Jacques Vasseur[3], Françoise Debart[3], Jean-François Eléouët[1,*], and Marie Galloux[1,*]

From the [1]INRAE, UVSQ, VIM, Université Paris-Saclay, Jouy-en-Josas, France; [2]CEA, CNRS, IBS, University of Grenoble Alpes, Grenoble, France; and [3]IBMM, ENSCM, CNRS, UMR, Université de Montpellier, Montpellier, France

Edited by Karin Musier-Forsyth

Respiratory syncytial virus has a negative-sense single-stranded RNA genome constitutively encapsidated by the viral nucleoprotein N, forming a helical nucleocapsid which is the template for viral transcription and replication by the viral polymerase L. Recruitment of L onto the nucleocapsid depends on the viral phosphoprotein P, which is an essential L cofactor. A prerequisite for genome and antigenome encapsidation is the presence of the monomeric, RNA-free, neosynthesized N protein, named N^0. Stabilization of N^0 depends on the binding of the N-terminal residues of P to its surface, which prevents N oligomerization. However, the mechanism involved in the transition from N^0-P to nucleocapsid assembly, and thus in the specificity of viral genome encapsidation, is still unknown. Furthermore, the specific role of N oligomerization and RNA in the morphogenesis of viral factories, where viral transcription and replication occur, have not been elucidated although the interaction between P and N complexed to RNA has been shown to be responsible for this process. Here, using a chimeric protein comprising N and the first 40 N-terminal residues of P, we succeeded in purifying a recombinant N^0-like protein competent for RNA encapsidation *in vitro*. Our results showed the importance of RNA length for stable encapsidation and revealed that the nature of the 5′ end of RNA does not explain the specificity of encapsidation. Finally, we showed that RNA encapsidation is crucial for the *in vitro* reconstitution of pseudo-viral factories. Together, our findings provide insight into respiratory syncytial virus viral genome encapsidation specificity.

The *Mononegavirales* order includes many human pathogenic viruses such as those responsible for rabies, measles, mumps, haemorrhagic fevers due to Ebola or Nipah viruses, and respiratory diseases induced by human respiratory syncytial virus (HRSV), metapneumovirus (HMPV), or parainfluenza viruses (1). All these viruses have a negative-sense single-stranded RNA genome that is constitutively encapsidated by the nucleoprotein N, forming the nucleocapsid (NC). This NC serves as a template for the viral polymerase L responsible for both viral transcription and replication (2, 3). For the vast majority of these viruses, transcription and replication are cytoplasmic, occurring in viral factories which are viro-induced organelles called inclusion bodies (IBs) (4–8).

Among *Mononegavirales*, HRSV is the prototype of the *Pneumoviridae* family and the *Orthopneumovirus* genus (9, 10). HRSV is the most common cause of acute lower respiratory infections in young children worldwide (11–13). It is also recognized as a major cause of severe respiratory infections in immunocompromised and elderly people (14–16). Currently, no vaccine is available, and the only specific treatment against HRSV is prophylactic, consisting of injection of humanized monoclonal antibodies directed against the fusion protein F (palivizumab, Sinagis) (17). However, the efficacy of this treatment is controversial and its high cost limits its prescription to at-risk children. The HRSV genome is approximatively 15.2 kb long and contains 10 genes encoding 11 proteins (2). Replication and transcription rely on 4 of these proteins: the RNA-dependent RNA polymerase L which exhibits all the enzymatic activities required for viral replication and transcription, its cofactor, the phosphoprotein P responsible for the recruitment of L on the NC, the nucleoprotein N involved in genome and antigenome encapsidation, and the transcription factor M2-1 that has been described as an "antiterminating" factor during transcription and interacts with P and viral mRNA.

During transcription, the polymerase L recognizes the *leader* sequence at the 3′ end of the genome, and the polymerase is guided by the *gene start* (*gs*) and *gene end* (*ge*) sequences flanking each gene in the viral genome. The neosynthesized viral mRNAs are capped and methylated at the 5′ end and polyadenylated at the 3′ end by the polymerase. It is noteworthy that the synthesis of all viral mRNAs depends on the presence of the M2-1 protein, which is required for L processivity along the genome (18, 19). The mechanism of action of M2-1 is still poorly understood. However, it has recently been shown that RSV mRNAs concentrate with M2-1 in specific subcompartments of IBs called IBs-associated granules (8), suggesting that the M2-1–mRNA interaction may promote the release of mRNAs from the polymerase L.

On the contrary, replication of the viral genome only depends on L, P, and the NC. In that case, the polymerase

* For correspondence: Marie Galloux, marie.galloux@inrae.fr; Jean-François Eléouët, jean-francois.eleouet@inrae.fr.

recognizes the *leader* or the *trailer* sequences at the 3′ end of the genome or antigenome respectively, and the RNA synthesis starts at the first nucleotide and the polymerase proceeds through the *ge* and *gs* sequences to the end of the genome (or antigenome) (20, 21). Genomes and antigenomes, which have a triphosphate 5′ end (22, 23), are directly encapsidated by the N protein during their synthesis, forming helical NC (24) which can both be incorporated in progeny virions (25, 26). Encapsidation of genome and antigenome thus prevents the formation of double strand RNAs but also their degradation as well as their detection by cellular sensors of the innate immune system. The structure of N expressed in *Escherichia coli* and purified as N-RNA rings composed of 10 protomers revealed that each N protomer interacts with 7 nucleotides (27). The RNA binds within a groove formed by the interface between the 2 globular domains of N (N_{NTD} and N_{CTD}) that are separated by a flexible hinge region. The N protein also possesses 2 N- and C-terminal extensions (N- and C-arms) that are involved in N oligomerization: the N-arm of the N_i protomer binds to the N_{i-1} protomer, whereas the C-arm of N_i binds to the top of the N_{CTD} of the N_{i+1} protomer (24, 27). RNA encapsidation therefore depends on both direct interaction with RNA and the ability of N to oligomerize, 2 mechanisms that are closely coupled. When expressed alone, the *Mononegavirales* N proteins all show a strong tendency to encapsidate cellular RNAs. This implies that viral replication depends on the ability to maintain a pool of RNA-free monomeric N, termed N^0, available for the specific encapsidation of genomic and antigenomic RNAs. It is now well established that all these viruses share a common mechanism, with the neosynthesized N being maintained in the N^0 form by P which acts as a molecular chaperone (28–36). Specifically for HRSV, and by analogy to the N^0–P complex of the HMPV whose crystal structure has been solved (31), the binding of the 28 N-terminal residues of P to the N_{CTD} surface overlaps with the binding sites of both the N- and C-arms of the N_{i+1} and N_{i-1} protomers in the oligomeric form, preventing self-oligomerization of N (30, 37). Notably, N^0 is characterized by a rotation of N_{NTD} relative to N_{CTD} compared to the oligomeric form and a stacking of the C-terminal arm of N into the positively charged RNA groove that blocks RNA binding (30). However, the mechanism involved in the switch from N^0 to N-RNA, which regulates specific encapsidation of genomes and antigenomes remains poorly characterized.

In addition to their critical role in viral polymerase function, N and P have been shown to be the scaffold proteins responsible for IBs morphogenesis (38, 39). It has recently been shown that IBs are liquid organelles formed by liquid-liquid phase separation induced by N–P interaction (39, 40). Importantly, the P protein (241 residues long), which forms tetramers through its central oligomerization domain (residues 131–151) flanked by highly disordered N- and C-terminal domains (P_{NTD} and P_{CTD} respectively) that are involved in multiple protein–protein interactions, plays a central role in regulating polymerase activity as well as in IBs formation. The P_{NTD} interacts with N^0 (37), M2-1 (41), the cellular phosphatase PP1 (41), and the viral matrix protein M responsible for virion assembly (42), whereas P_{CTD} is involved in the interaction with L (43, 44) and NC (45, 46) and is critical for IBs formation (39). Both the length of the P_{CTD} and its interaction with N complexed to RNA are required for efficient IBs morphogenesis. However, the importance of N oligomerization and of RNAs in the morphogenesis of IBs remains to be characterized.

In this study, we investigated the specificity of RNA encapsidation by HRSV N. Using a fusion protein between the full-length N and the peptide derived from the first 40 N-terminal residues of P (P40) responsible for chaperone activity on N^0, we managed to purify a recombinant monomeric and RNA-free N-P40 chimeric protein. The resulting N-P40 protein was competent for *in vitro* RNAs encapsidation, the length of RNAs being critical for stable oligomerization, and invariably leading to the formation of N-RNA rings under the conditions tested. Furthermore, using this N-P40 protein, we revealed that RNA encapsidation is critical for the morphogenesis of pseudo-IBs *in vitro*.

Results

Production of a N^0-like recombinant protein

Recently, a strategy based on coexpression of P_{NTD} with His-tagged N in *E. coli* allowed the purification of a N^0–P_{NTD} complex competent for encapsidation (47). Given the low affinity of P peptide for N (37), which could lead to the loss of peptide upon purification and thus to N aggregation, we chose here to use a strategy based on the expression of a fusion protein between His-tagged full-length N and the 40 N-terminal residues of P (P40) in *E. coli* (Fig. 1*A*). This approach was previously used to determine the crystal structure of the N^0–P complexes of HMPV (31), measles virus (34), and parainfluenza virus 5 (32). After purification of this chimeric protein in the presence of 1 M NaCl, the sample was analyzed by size-exclusion chromatography, following the absorbance at 260 and 280 nm, and compared to the profile of purified WT N (N_{wt}) forming N-RNA rings (46). The elution profile of N-P40 showed 2 peaks (Fig. 1*B*). The major P1 peak with A_{260nm}/A_{280nm} ratio >1 and apparent mass of ∼500 kDa (estimated from the Superdex 200 calibration profile), of slightly smaller size than N-RNA rings, that could correspond to N-RNA oligomers or aggregates. A minor P2 peak presented A_{260nm}/A_{280nm} ratio <1 and apparent mass of ∼50 kDa, as expected for monomeric RNA-free N-P40 protein. The fractions of P1 or P2 peaks were pooled, and samples were analyzed by SDS-PAGE stained with Coomassie blue and by band shift assay on native agarose gel and compared to the sample corresponding to purified N_{wt}. As shown on Figure 1*C* (upper panel), as analyzed by SDS-PAGE, the presence of a single band with a molecular weight close to 45 kDa for N_{wt} sample and of 50 kDa for P1 and P2 peaks were observed, consistent with the expected mass of the N_{wt} and the N-P40 protein, respectively. On native agarose gel, the N_{wt} complexed to RNA and thus negatively charged clearly migrated within the gel. The N-P40 from the P1 peak migrated with a single band, close to the band observed for N_{wt}, suggesting that N-P40 could

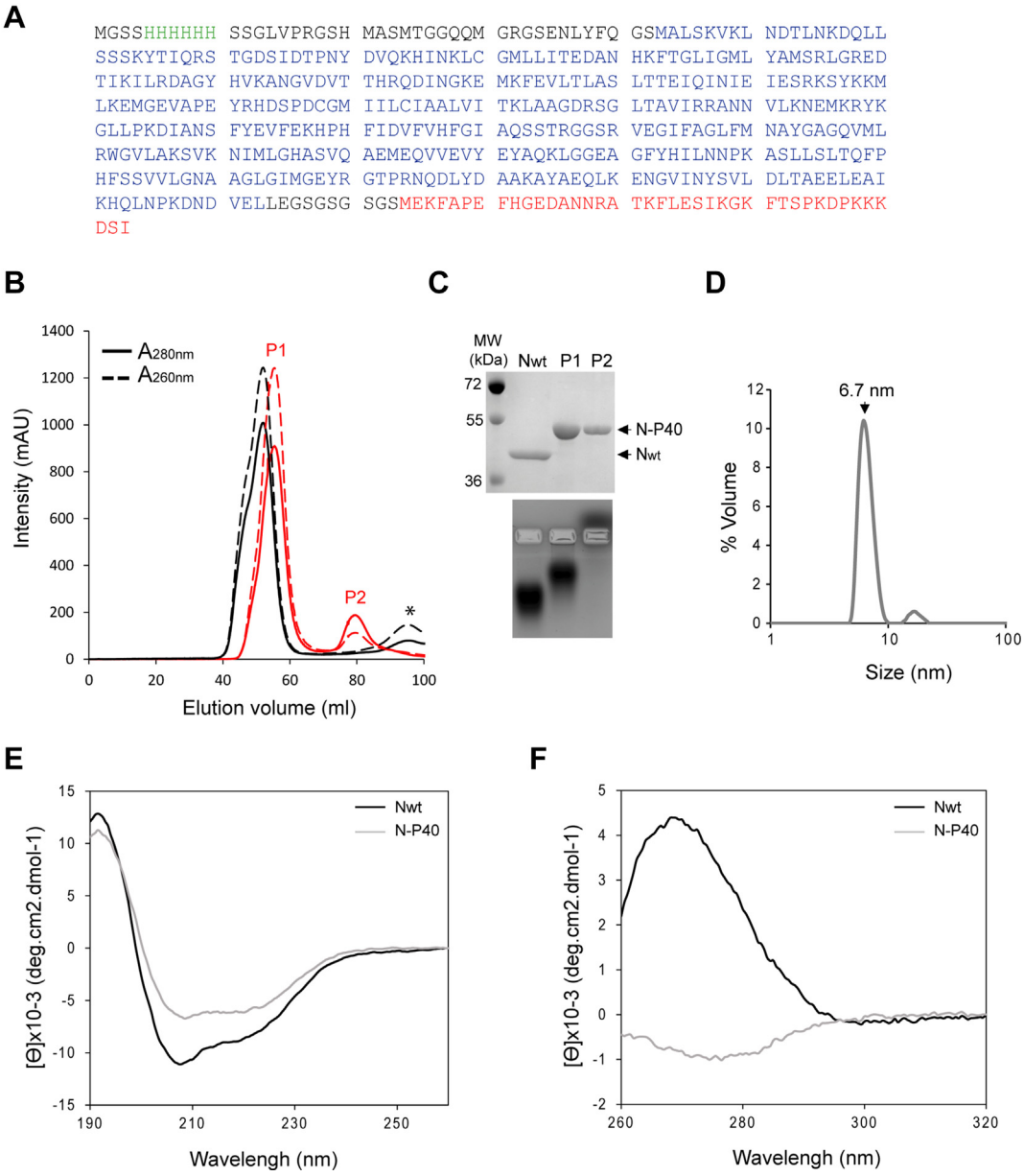

Figure 1. Purification and characterization of recombinant N-P40 fusion protein. *A*, amino acid sequence of the N-P40 fusion protein. The N-terminal 6xHis tag is in *green*, the N sequence is in *blue*, and the sequence of P40 is in *red*. Amino acids in *black* correspond to additional residues and linkers. *B*, gel filtration profile of purified N-P40 (*red*) and N_{wt} (*black*). The curves corresponding to absorbance at 260 nm and 280 nm are presented as *dash* and *solid lines*, respectively. P1 and P2 indicate the 2 peaks detected for the gel filtration profile of N-P40. The asterisk indicates the peak corresponding to the C-terminal fragment of P used for N_{wt} purification (46). *C*, the fractions corresponding to the peak of purified N_{wt} and to the peaks P1 and P2 of the gel filtration profile of N-P40 were pooled, and the samples were analyzed by SDS-PAGE colored with *Coomassie blue* (*upper* panel) and by migration on native agarose gel (*lower* panel). *D*, dynamic light scattering (DLS) analysis of the N-P40 protein isolated from the gel filtration peak P2, showing a homogenous peak close to 6.7 nm, corresponding to N-P40 monomer and a minor peak of oligomers. *E* and *F*, far-UV (*E*) and near-UV CD (*F*) spectra of N_{wt} corresponding to N-RNA rings in *black* and N-P40 in *gray*.

oligomerize as rings (Fig. 1*C*, lower panel). On the contrary, N-P40 from the P2 peak poorly migrated within the gel and in the opposite direction.

We then focused on the sample from P2 peak which was dialyzed to 300 mM NaCl and concentrated up to 1.5 mg/ml. Dynamic light scattering (DLS) analysis of the sample revealed the presence of a major protein peak near 6.7 mm in diameter that should correspond to monomers and a minor peak of oligomers near 17 nm in diameter (Fig. 1*D*). These data revealed that in our conditions, N-P40 tended to aggregate or oligomerize upon concentration and led us to work with a protein concentration of 1 mg/ml. We finally analyzed the secondary and tertiary structures of N-P40 by circular dichroism (CD), using as previously N_{wt} purified as N-RNA rings as a control. The far-UV spectra of both N-P40 and N_{wt} showed peaks at 208 and 222 nm, typical of secondary structures with predominant α-helical content (Fig. 1*E*). The peak intensity shift observed for N-P40 revealed a lower helical content than N_{wt}. This observation correlates with the insertion of linkers in the N-P40 constructs, which are expected to

be unfolded. The near-UV CD allows the detection of signals from aromatic residues engaged in a rigid chiral environment, consistent with the presence of a tertiary structure. The detection of a broad signal around 280 nm for the N-P40 protein can be attributed to the signal from Tyr and Trp residues and validates that the protein has a tertiary structure (Fig. 1*F*). In comparison, the spectrum obtained for N_{wt} revealed an intense positive signal between 260 and 280 nm, which can be attributed to the presence of RNA masking the signals from the aromatic residues of N.

Overall, these results show that N-P40 can be purified as a monomeric and RNA-free protein and that the fusion of P40 does not have a major impact on N folding. This latter observation correlates with previous results showing that binding of P40 to N does not induce major conformational changes in N (30).

N-P40 is competent for encapsidation of RNAs

We then assessed the capacity of the N-P40 protein to encapsidate RNA *in vitro*. As each N_{wt} protomer has been shown to interact with seven nucleotides within purified N-rings formed of 10 or 11 protomers (27), we first tested the ability of N-P40 to encapsidate a 70-nucleotide long (70-mer) RNA or DNA of similar sequence. The RNA sequence that we used was the antileader sequence (the 5′ end of the antigenomic RNA), which is the initial RNA sequence synthetized by the polymerase using the genomic RNA as a template (Table 1). Encapsidation of RNA by N-P40 was analyzed using a band shift assay on native polyacrylamide and agarose gels, using N_{wt} rings as a control. As shown in Figure 2*A*, while only slight migration was observed for purified N-P40, a clear band shift was observed when N-P40 was incubated with RNA. However, the protein seemed to poorly interact with DNA. In parallel, the samples were observed by negative stain electron microscopy (ns-EM). As expected, images of N-P40 alone showed only very small species (Fig. 2*C*). While N-P40 incubated with 70-mer RNA formed ring-shaped N-RNA assemblies, only aggregates were observed for the sample of N-P40 incubated with DNA (Fig. 2*C*). These results suggest that, although N could interact with DNA, the affinity is not sufficient to allow the regular and constrained assembly of N on nucleotides, which, based on the crystal structure, implies twists on the ribose-phosphate chain (27). Using the same approach, we confirmed that N-P40 was also capable of encapsidating shorter 14-mer RNAs and forming N-RNA rings (Fig. 2, *B* and *C*). Furthermore, as the first nucleotides could initiate RNA encapsidation, we investigated the impact of substitutions of the 2 first nucleotides on the capacity of N to encapsidate 14-mer RNAs (Table 1). However, we observed that N-P40 similarly encapsidated 14-mer RNAs of different sequences (Fig. 2*B*), suggesting that the first nucleotides are not critical for starting RNA encapsidation.

Our results thus show that, although fused to N, the P40 peptide is not sufficient to prevent RNA encapsidation *in vitro*. Furthermore, while N-P40 specifically encapsidated RNAs over DNA, no specificity in RNA length was observed under the conditions tested. It is noteworthy that, as previously observed by Gao *et al.* (47), *in vitro* encapsidation of RNA did not result in the formation of helical NCs but only in N-RNA rings.

Investigation of the minimal RNA length required for encapsidation

Using the same antileader sequence of HRSV, we further studied the minimal RNA length required for encapsidation, using 5- to 11-mer oligonucleotides (Table 1). As shown in Figure 3*A*, no band shift of N-P40 was detected on native polyacrylamide or agarose gels in the presence of 5- and 6-mer

Table 1
RNAs sequences

RNAs length	5′ end modification	RNA sequence[a]
70-mer[b]	OH	5′-ACGCGAAAAAAUGCGUACAACAAACUUGCAUAAACCAAA AAAAUGGGGCAAAUAAGAAUUUGAUAAGUAC-3′
14-mer (a)		5′-ACGCGAAAAAAUGC-3′
14-mer (b)		*5′-GGGCGAAAAAAUGC-3′*
14-mer (c)		*5′-GUGCGAAAAAAUGC-3′*
11-mer		5′-ACGCGAAAAAA-3′
10-mer		5′-ACGCGAAAAA-3′
9-mer		5′-ACGCGAAAA-3′
8-mer		5′-ACGCGAAA-3′
7-mer		5′-ACGCGAA-3′
6-mer		5′-ACGCGA-3′
5-mer		5′-ACGCG-3′
11-mer	ppp	5′-ACGCGAAAAAA-3′
10-mer		5′-ACGCGAAAAA-3′
9-mer		5′-ACGCGAAAA-3′
8-mer		5′-ACGCGAAA-3′
7-mer		5′-ACGCGAA-3′
11-mer	^{7m}Gppp	5′-ACGCGAAAAAA-3′
10-mer		5′-ACGCGAAAAA-3′
9-mer		5′-ACGCGAAAA-3′
8-mer		5′-ACGCGAAA-3′
7-mer		5′-ACGCGAA-3′

[a] All the sequences correspond to HRSV antileader sequence except those of the 14-mer b and c indicated in italics.
[b] Corresponding 70-mer DNA was used in the study.

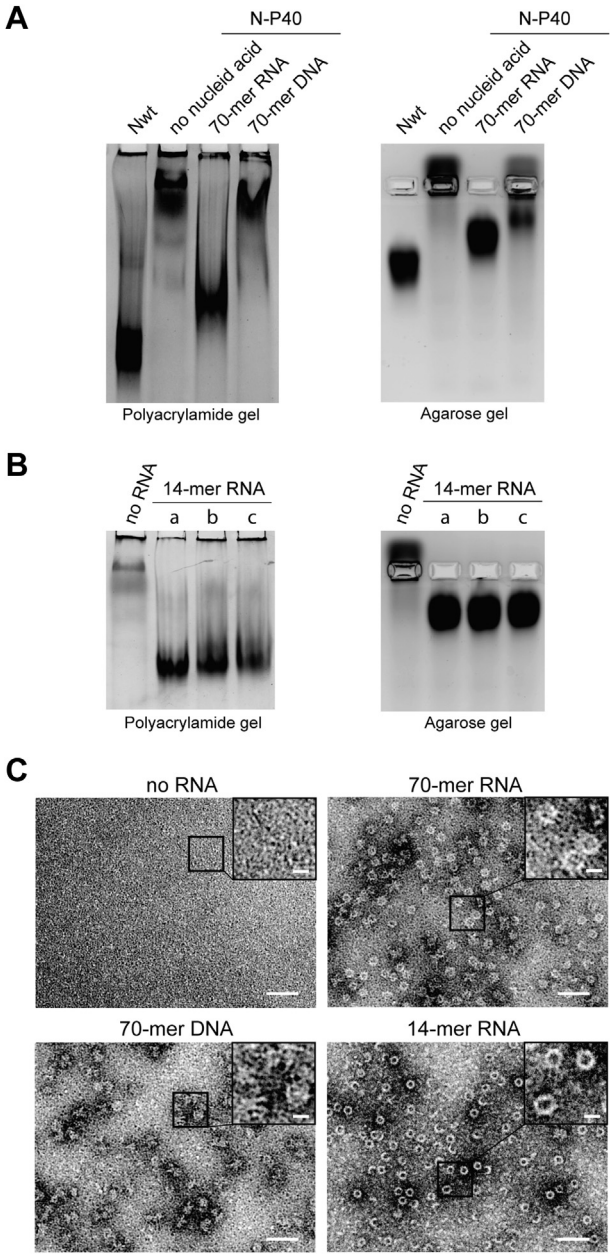

Figure 2. The N-P40 fusion protein is competent for RNA encapsidation. *A*, analysis of N-P40 migration alone or incubated in the presence of 70-mers RNA or DNA (see 70-mer sequence in Table 1) by native polyacrylamide (*left*) or agarose (*right*) gel electrophoresis. Polyacrylamide and agarose gels were stained with *Coomassie blue* or *amido black* respectively. N_{wt} corresponds to purified recombinant RNA-N rings, used as control. *B*, analysis of 14-mer RNAs (see sequences Table 1) encapsidation by N-P40 on native polyacrylamide (*left*) or agarose (*right*) gels. *C*, images of N-P40 alone or incubated in the presence of 70-mer RNA, 70-mer DNA, or 14-mer RNA, as observed by ns-EM. The scale bar represents 50 nm. Magnifications of selected areas (indicated by *black squares*) are presented at the right top of each panel. The scale bar represents 10 nm. ns-EM, negative stain electron microscopy.

RNAs. Similar N-P40 band shifts were observed in the presence of 10- and 11-mer oligonucleotides compared with N-P40 incubated with 14-mer RNAs. Finally, intermediate band shift profiles were observed for N-P40 incubated in the presence of 7-, 8-, and 9-mer RNAs. Yet, according to ns-EM observations, incubation of N-P40 with 7-mer and 11-mer RNAs both led to the formation of N-RNA rings, similar to the ones observed with the 14-mer and 70-mer RNAs (Fig. 3*B*). To clarify these results, we next investigated the stability of the N-P40–RNA complexes by incubating the samples overnight in the presence of RNase A followed by dialysis. Migration analysis of the samples on a native agarose gel showed no band shift for N-P40 incubated with 6- to 10-mer RNAs, suggesting RNA digestion, whereas a band shift was still observed for N-P40 in the presence of 11-mer and 14-mer RNAs (Fig. 3*C*), indicating that RNA was protected from digestion. Further analysis of the samples was performed by measuring the A_{260nm}/A_{280nm} ratio and by investigating structural changes of N-P40 by DLS and near-UV CD. Before RNase A treatment, all samples displayed an A_{260nm}/A_{280nm} ratio close to 1.2, similar to the value measured for N_{wt} (Table 2). After RNase A treatment, A_{260nm}/A_{280nm} ratios were <1 for N-P40 samples incubated with 6- to 10-mer RNAs (Table 2), validating RNA digestion upon RNase A treatment. Of note, the A_{260nm}/A_{280nm} ratio of these samples remained higher than that obtained for purified N-P40. For N-P40 incubated in the presence of 11- and 14-mer RNAs, the A_{260nm}/A_{280nm} ratios were close to 1. These data suggested that, although the RNAs were partially digested by RNase A, N-P40 was still associated with RNAs, preventing complete RNA degradation. In parallel, determination of the hydrodynamic diameter (Dh) of the samples by DLS revealed that N-P40 incubated in the presence of 6- to 10-mer RNAs displayed a Dh between 6.7 and 9 nm after RNase treatment, close to the Dh obtained under the same conditions for N-P40 alone, whereas those of N-P40 incubated with 11- and 14-mer RNAs were 14.2 and 14.4 nm, respectively, similar to the Dh of N_{wt} (Table 2). Furthermore, the near-UV CD spectra showed that only the N-P40 sample incubated with 11-mer RNA exhibited a positive peak around 260 nm, whereas the spectra with 7- to 10-mer RNAs were similar to purified N-P40 alone or displayed only a weak signal around 260 nm (Fig. 3*D*). These data correlate with absorbance and Dh measurements, suggesting that RNase A treatment induced degradation of RNAs shorter than 11-nucleotides long and N rings disassembly.

Altogether, these results reveal that stable RNAs encapsidation by N-P40 depends on RNA length, with the minimal length to stabilize N-P40–RNA complexes being 11-mer RNAs.

Impact of 5′end modification of RNAs on encapsidation

One of the differences between RNAs lies in post-transcriptional modifications, notably at the 5′end. Genomic and antigenomic RNAs have been described as having a 5′ triphosphate (ppp) (22, 23), whereas viral mRNAs are capped and methylated by L during their synthesis (3). Therefore, we investigated whether posttranscriptional modifications of the 5′ end of RNAs could impact the ability of N to encapsidate RNAs. Again, N-P40 was incubated in the presence of synthetic 7- to 11-mer RNAs with either a 5′ ppp or a *N*7 and 2′-*O* methylated cap structure (^{7m}Gppp) (Table 1), followed by native agarose gel electrophoresis

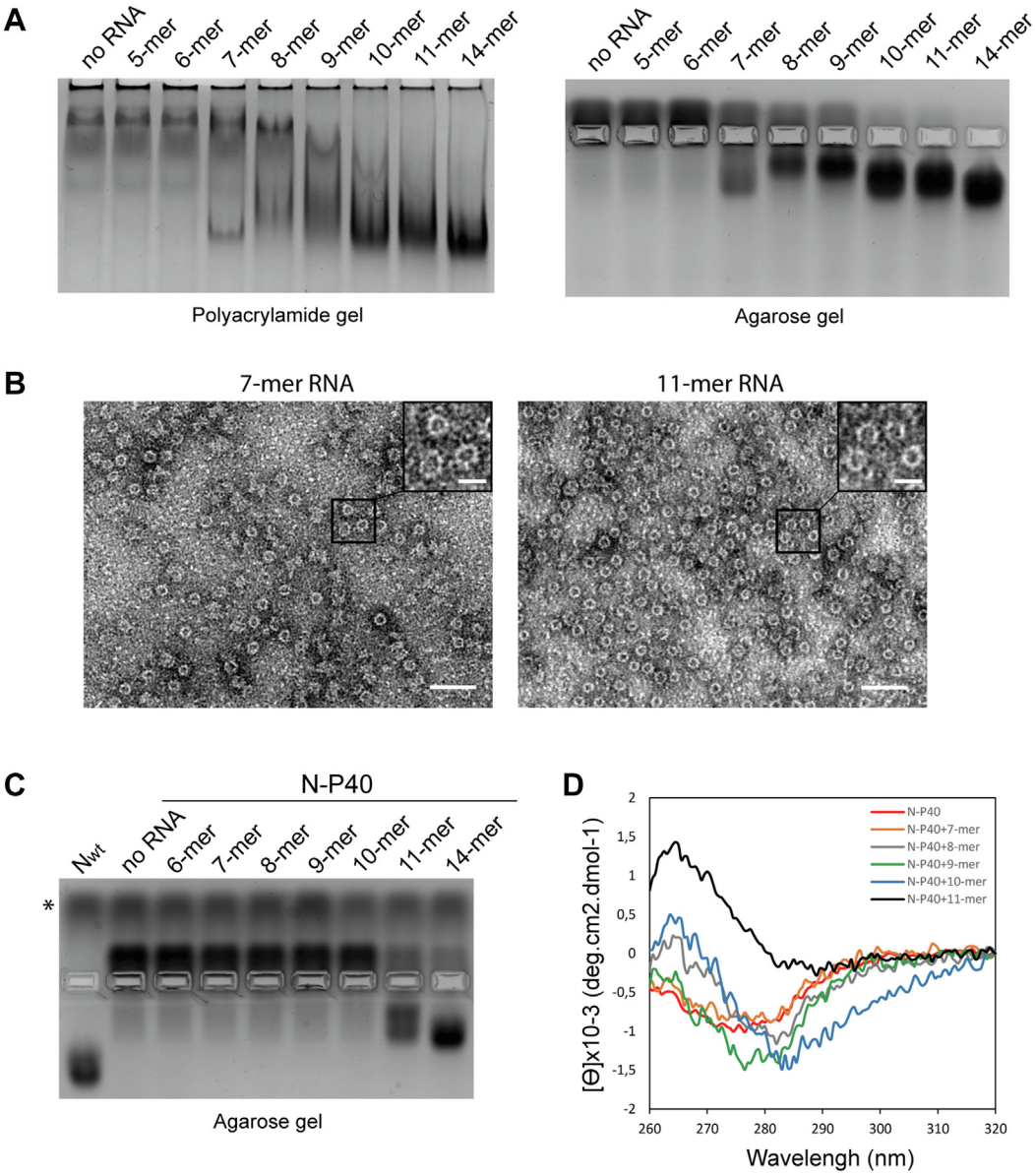

Figure 3. Formation of stable RNA-N complexes by N-P40 depends on RNA length. *A*, analysis of N-P40 migration alone or incubated in the presence of 5- to 11-mer RNAs, compared to 14-mer RNAs, by native polyacrylamide (*left*) or agarose (*right*) gel electrophoresis. Polyacrylamide and agarose gels were stained with *Coomassie blue* or *amido black* respectively. *B*, images of N-P40–RNA complexes formed upon incubation of N-P40 in the presence of 7- and 11-mer RNAs with 5′ OH, as observed by ns-EM. The scale bar represents 50 nm. Magnifications of selected areas (indicated by *black squares*) are presented at the right top of each panel. The scale bar represents 20 nm. *C*, analysis of N-P40 migration alone or incubated in the presence of 5- to 11-mer RNAs, after treatment with RNase A, by native agarose gel electrophoresis. Gel was stained with amido black. The *asterisk* indicates the band corresponding to RNase A. *D*, near-UV CD spectra of N-P40 alone or incubated in the presence of 7- to 11-mer RNAs, after treatment with RNase A. ns-EM, negative stain electron microscopy.

analysis. Results showed that the presence of ppp or ^{7m}Gppp at the 5′ end inhibited the ability of N to encapsidate 7- and 8-mer RNAs compared to 5′ OH RNAs (Figs. 3*A* and 4*A*). However, N-P40 was still able to encapsidate 9-, 10-, and 11-mer RNAs, and no difference was observed between 5′ end ppp or capped RNAs. Interestingly, independently of the length and the capping of the RNAs, N-P40–RNA rings could always be detected by ns-EM (Fig. 4*B*), suggesting that this method of observation may stabilize ring-shaped assemblies and highlights the importance of using multiple complementary techniques for the analysis of RNA encapsidation by N.

One more time, we investigated the impact of RNAs' 5′ end modification on the stability of N-P40-11-mer RNA complexes upon RNase A treatment. Surprisingly, although band shifts were still observed (Fig. 4*C*), N-P40 samples incubated with 5′ ppp and 5′ ^{7m}Gppp RNAs displayed A_{260nm}/A_{280nm} ratios of 0.9 and 1, respectively, and DLS analysis revealed the presence of different populations (not shown). Furthermore, while the near-UV CD spectrum of N-P40 incubated with 5′ ^{7m}Gppp RNAs was similar to the spectrum of N-P40 complexed with 5′OH RNA, the spectrum of N-P40 incubated with 5′ ppp RNAs clearly differed from those of N-P40 alone or incubated with 5′ OH RNAs (Fig. 4*D*).

Table 2
Characterization of 5′ OH RNA–N-P40 complexes after RNase A treatment

Proteins and RNAs	A_{260nm}/A_{280nm}	Dh (nm)[a]
Nwt[b]	1.24	15.75
N-P40	0.67	7.9
N-P40 + 6-mer RNA	0.79	8.9
N-P40 + 7-mer RNA	0.9	8.7
N-P40 + 8-mer RNA	0.88	6.7
N-P40 + 9-mer RNA	0.87	7.6
N-P40 + 10-mer RNA	0.94	9
N-P40 + 11-mer RNA	1.03	14.2
N-P40 + 14-mer RNA	1	14.4

[a] Hydrodynamic diameter determined by DLS. Data representative of 2 independent experiments.
[b] Purified as N-RNA rings.

These results revealed that modification of the 5′ end of RNAs only partially impairs encapsidation but is not a critical factor for the specificity of encapsidation, 5′ end modifications delay RNAs encapsidation maybe by creating steric hindrance.

Impact of full-length P protein on the stability of RNAs encapsidation

As our results were obtained in the presence of only a short peptide of P, we then assessed if full-length P protein could modulate the stability of RNAs encapsidation. By analysis on native agarose gel, we first showed that coincubation of P with N-P40 allowed to observe the formation of a complex, revealing that P was able to interact with N-P40, although this interaction appeared weak compared to the interaction between P and N_{wt} (Fig. 5*A*). This result suggests that P could bind to N either by displacing P40 binding on N or through the binding of the C-terminal extremity of P on N_{NTD}. In the presence of 14-mer RNA, a band of strong intensity, similar to the band observed in presence of N_{wt}, was observed, showing that P does not prevent RNA encapsidation by N-P40. We therefore studied the impact of P on encapsidation depending on RNA length. As previously, no band shift was detected in the presence of 5- and 6-mers. In the presence of 7- to 9-mers, a band of weak intensity migrating slightly faster and at the same level than the bands of strong intensity observed in the presence of 10-, 11-, and 14-mers was observed (Fig. 5*B*, upper panel). These data reveal that in the presence of RNA, the full-length P does not improve the stability of the monomeric N compared to the P40 peptide. Of note, upon treatment with RNase A, the band observed in the presence of 8- and 9-mers was not detected, and a clear decrease of intensity of the band observed in the presence of 10-mer RNA was observed (Fig. 5*B*, lower panel). Finally, in the presence of 5′ end ppp or ^{7m}Gppp RNAs, a band of strong intensity was observed only in the presence of 11-mer RNAs.

Altogether, these results reveal that the presence of P does not drastically impact RNA encapsidation or the stability of the oligomers.

Role of RNA encapsidation on pseudo-IBs morphogenesis in vitro

We have previously shown that *in vitro* coincubation of purified recombinant fluorescent N-RNA rings (mCherry-N_{wt}) with P can lead to the formation of liquid droplets that exhibit properties similar to cellular IBs formed during infection. We also identified the key properties of P required for pseudo-IBs morphogenesis, that is, oligomerization, P_{CTD} length and flexibility, and interaction of the C-terminus of P with N (39). However, this study did not decipher the role of N oligomerization and of the presence of RNAs in this process. Furthermore, although our data suggested that the N/P ratio maybe important for optimal IBs formation, these results remained preliminary, and a systematic study of the impact of N/P ratio and concentration on the morphogenesis of IBs was missing. As phase separation is known to be facilitated by increased protein concentration (48–52), we here decided to limit the protein concentrations to avoid spontaneous pseudo-IBs formation. Using a fixed minimum concentration of 3.5 μM for mCherry-N_{wt} or P, the addition of the second partner at a 1:1 ratio allowed us to observe the formation of small droplets of 1 to 5 μm in diameter (Fig. 6). A fixed low P concentration limited the size and number of droplets that remained similar whatever the concentration of mCherry-N (Fig. 6*A*). On the other hand, in a fixed low N concentration condition, the number and size of droplets increased proportionally to the addition of P until reaching a plateau for a P/N ratio ≥4 (Fig. 6*B*). These results correlate with our previous observations (39) but also revealed that P concentration is a limiting factor for IBs formation.

To study the impact of N-P40 oligomerization in the presence of RNAs on pseudo-IBs morphogenesis, we then investigated whether pseudo-IBs could form when N-P40 was incubated with a 70-mer RNA in the presence of P-BFP. Since no droplets were observed with a 3 μM concentration of N-P40 in the presence of an excess of P-BFP (15 μM) and 70-mer RNA at 50 μM, we then screened for the optimal conditions allowing pseudo-IBs formation, with a minimum concentration of proteins. Pseudo-IBs of 10 to 15 μm in diameter were observed in the presence of 3.5 μM of P-BFP, 70-mer RNAs (50 μM), and a minimum of 4-fold excess of N-P40 (13.5 μM). Of note, pseudo-IBs of only 2 to 3 μm in diameter were observed when coincubating P-BFP with N_{wt} (RNA-N rings) in the same conditions (Fig. 7*A*). It is noteworthy that no droplets were detected when incubating P-BFP in the presence of either RNAs or N-P40 alone (Fig. 7*A*). We then assessed the impact of RNA length on pseudo-IBs morphogenesis by incubating N-P40 with RNAs of various lengths before the addition of P-BFP, under the same conditions. As shown in Figure 7*B*, the addition of 14-mer RNA resulted in the formation of droplets similar to those observed in the presence of 70-mer RNA. More interestingly, droplet size decreased when N-P40 was incubated with 11-mer and 8-mer RNAs, and only aggregates were observed in the presence of 6-mer RNA. Furthermore, whereas RNase A treatment of N-P40 incubated with 11-mer RNA still allowed to observe droplets, only aggregates were detected for the sample with 8-mer RNA (Fig. 7*C*). This result correlates with data showing the instability of N oligomerization in the presence of short RNAs. Finally, pseudo-IBs similar to those obtained in the presence of

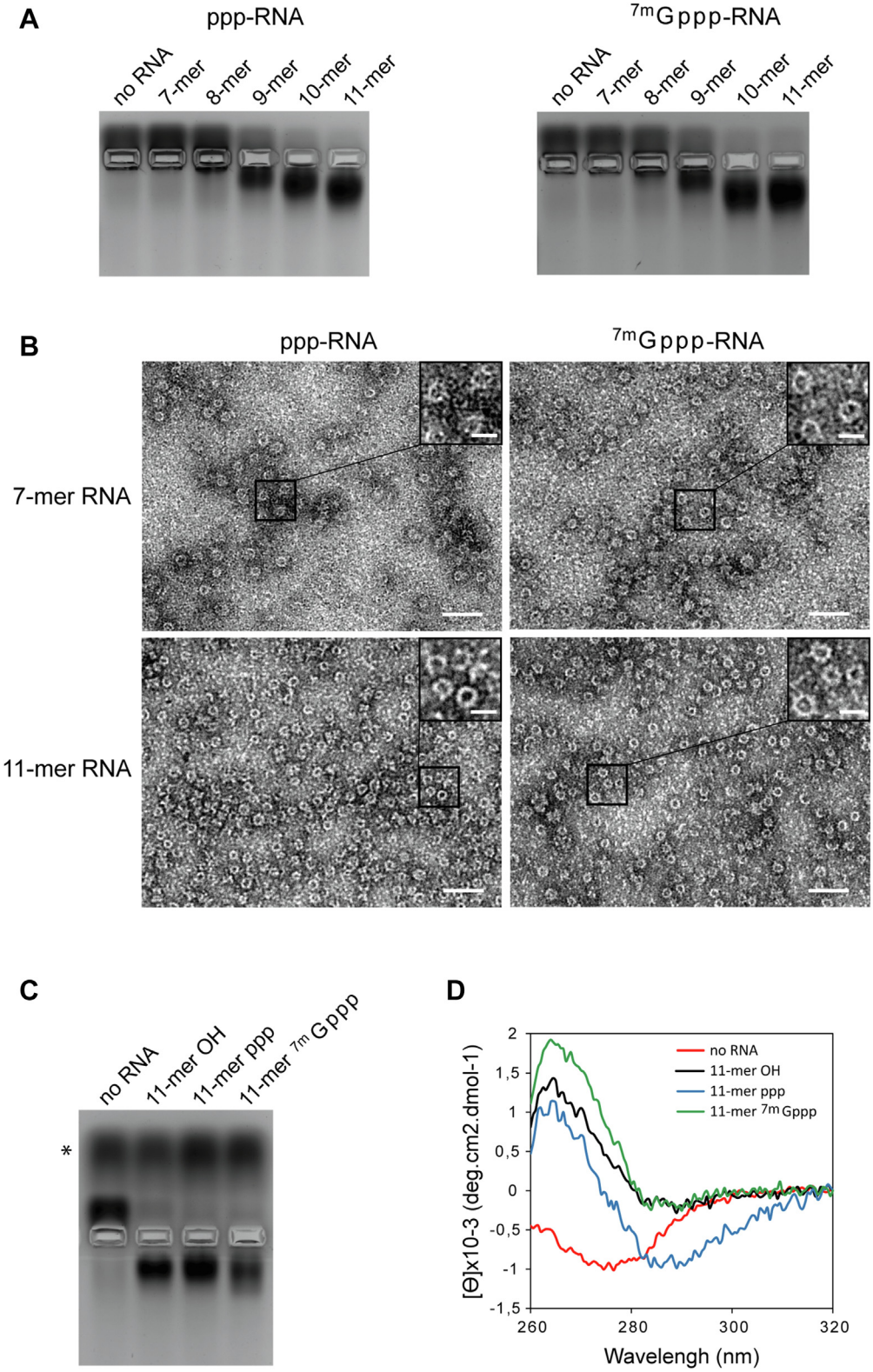

Figure 4. Impact of RNA 5′ end modifications on the ability of N-P40 to encapsidate RNAs. *A*, analysis of N-P40 migration alone or incubated in the presence of 7- to 11-mer RNAs with 5′ ppp (*left*) or 5′^{7m}Gppp (*right*) by native agarose gel electrophoresis. Gels were stained with *amido black*. *B*, images of N-P40–RNA complexes formed upon incubation of N-P40 in the presence of 7- and 11-mer RNAs with 5′ ppp or 5′ ^{7m}Gppp, as observed by ns-EM. The scale bar represents 50 nm. Magnifications of selected areas (indicated by *black squares*) are presented at the right top of each panel. The scale bar represents 20 nm. *C*, comparison of the migration of N-P40 alone or incubated in the presence of 11-mer RNAs with 5′ OH, ppp, or ^{7m}Gppp after RNase A treatment by native agarose gel electrophoresis, gel stained with amido black. *D*, near-UV CD spectra of N-P40 alone or incubated in the presence of 11-mer RNAs with 5′ OH, ppp, or ^{7m}Gppp after RNase A treatment. ns-EM, negative stain electron microscopy.

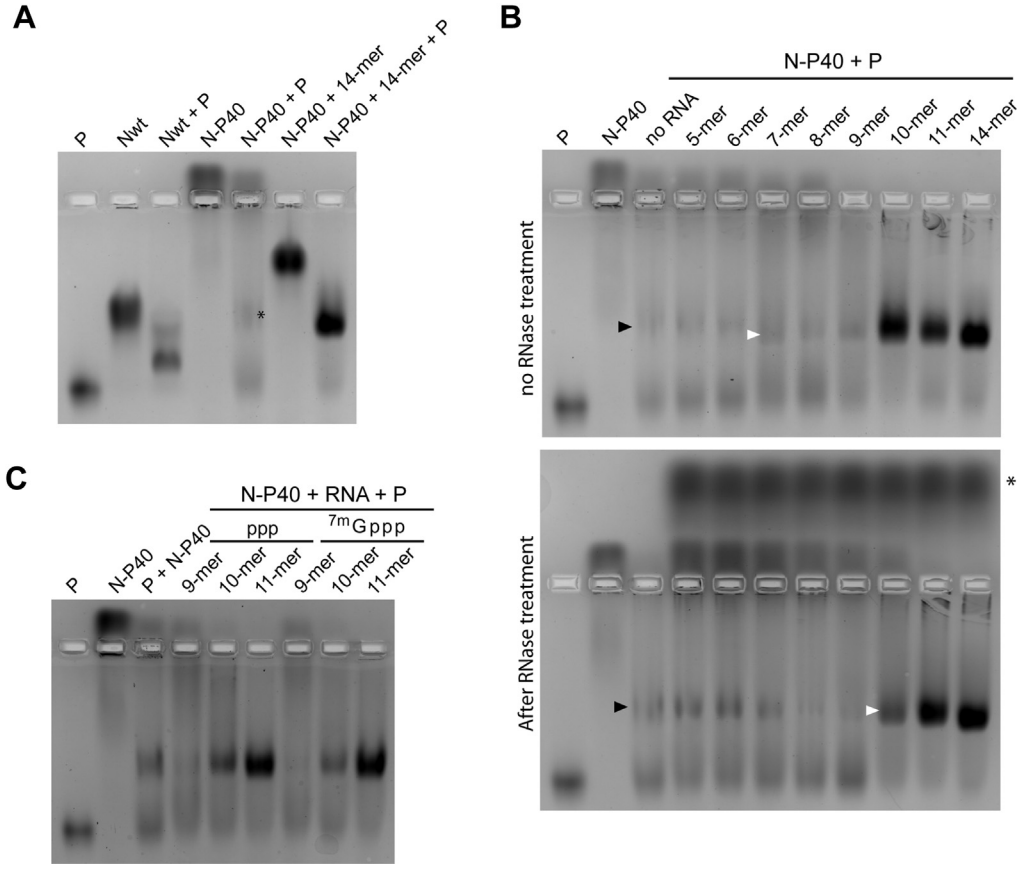

Figure 5. Impact of full-length P on the stability of RNA encapsidation. *A*, migration on native agarose gel of P, N_{wt}, or N-P40 in the absence or presence of 14-mer RNA alone or coincubated in the absence or the presence of 14-mer RNA. The *asterisk* indicates the band corresponding to P–N-P40 complex migration. *B* and *C*, analysis by native agarose gel electrophoresis of P and N-P40 migration alone or incubated in the presence of 7- to 11-mer RNAs (*B*) before (*upper panel*) or after treatment (*lower panel*) by RNase A or with 9- to 11-mer RNAs displaying 5′ ppp or ^{7m}Gppp (*C*). The *black* and *white* arrows indicate the bands corresponding the migration of P–N-P40 and P–N-P40–RNA complexes, respectively. The *asterisk* indicates the band corresponding to RNase A.

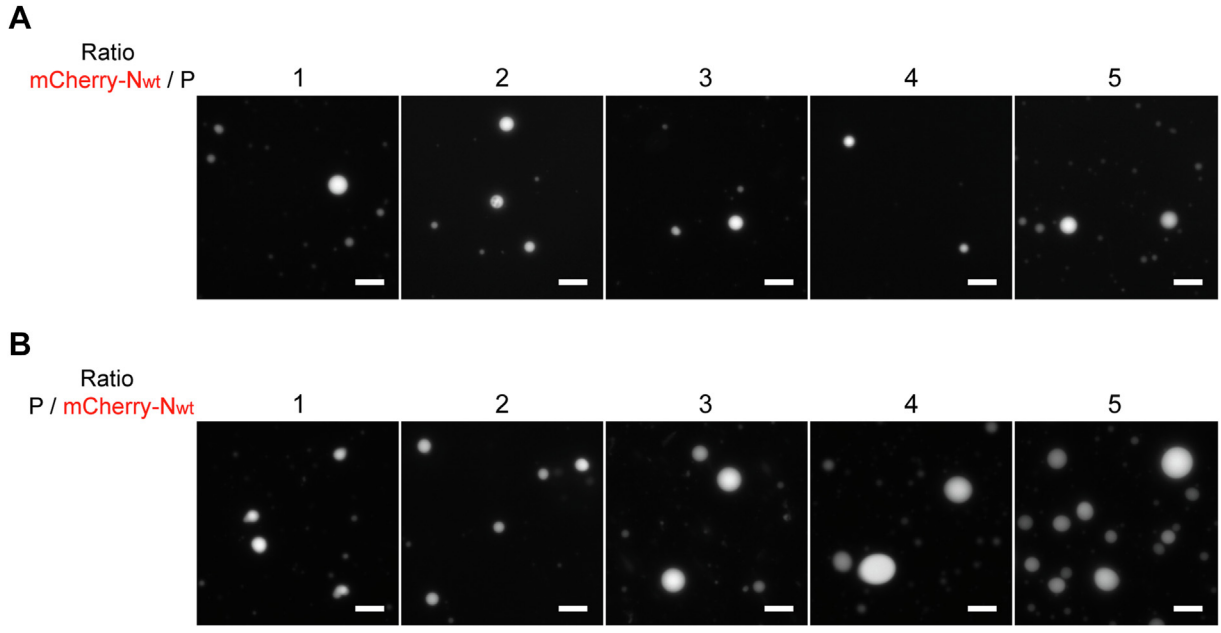

Figure 6. Impact of N_{wt} and P concentration and ratio on pseudo-IBs formation. Recombinant mCherry-N_{wt} (corresponding to mCherry-N-RNA rings) and P proteins were coincubated in the presence of 15% Ficoll and the formation of droplets was observed by fluorescence microscopy. *A*, P concentration was fixed to 3.5 μM, and mCherry-N_{wt} was added up to a ratio mCherry-N_{wt}/P of 5; *B*, mCherry-N_{wt} concentration was fixed to 3.5 μM, and P concentration increased up to a ratio P/mCherry-N_{wt} of 5. The scale bar represents 10 μm. IB, inclusion body.

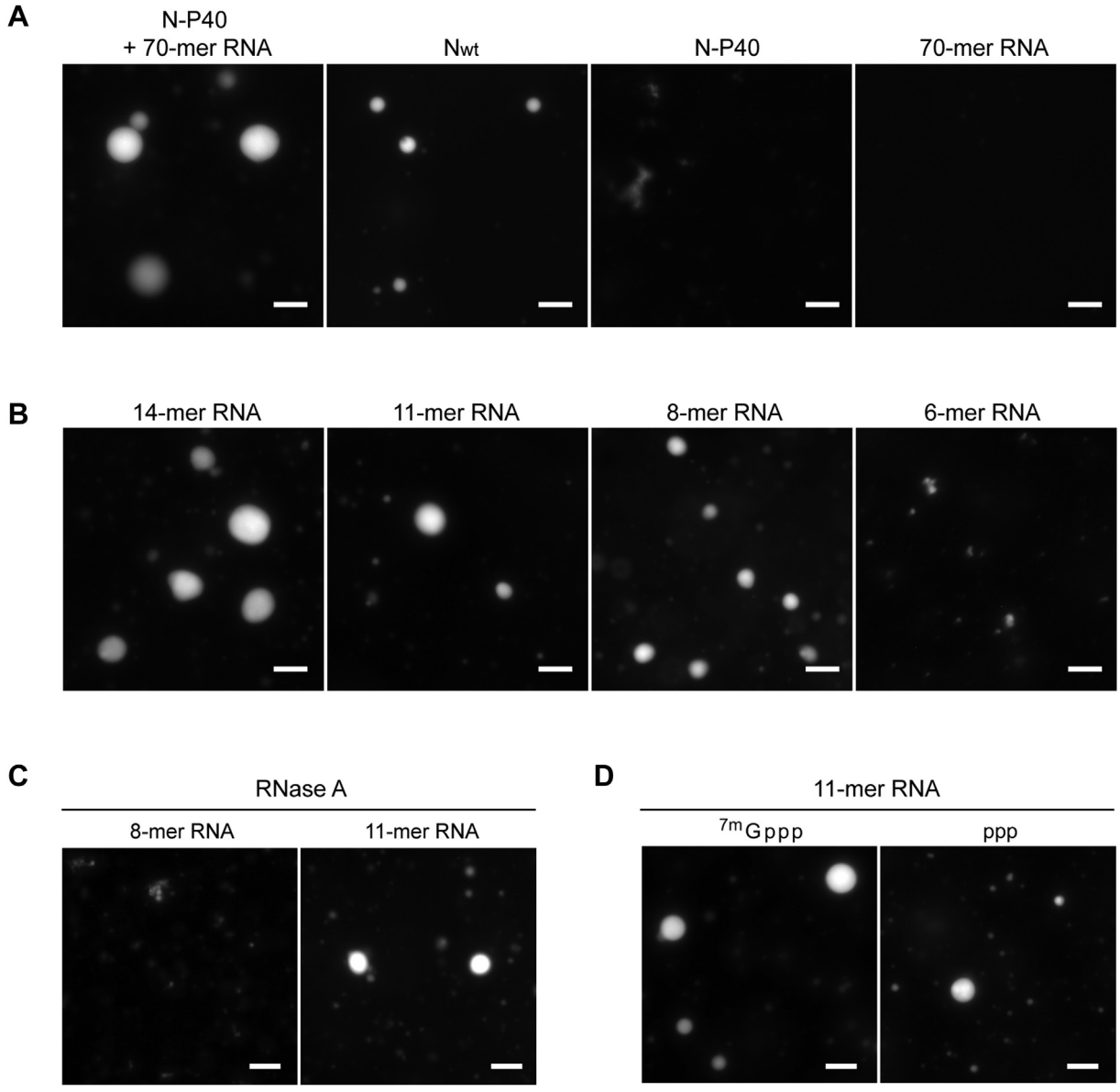

Figure 7. N oligomerization is needed for the formation of pseudo-IBs. *A*, recombinant P-BFP (3.5 μM) was incubated in the presence of either N-P40 preincubated with 70-mer RNA (13.5 and 50 μM, respectively), N_{wt} (13.5 μM), N-P40 (13.5 μM), or 70-mer RNA (50 μM). *B*, recombinant P-BFP (3.5 μM) was incubated in the presence of N-P40 (13.5 μM) preincubated with 14-mer, 11-mer (5′ end OH), 8-mer, or 6-mer RNAs (50 μM). *C*, recombinant P-BFP (3.5 μM) was incubated in the presence of N-P40 (13.5 μM) preincubated with 8-mer and 11-mer RNAs (50 μM) followed by treatment with RNAse A. *D*, recombinant P-BFP (3.5 μM) was incubated in the presence of N-P40 (13.5 μM) preincubated with 5′ ppp or ^{7m}Gppp 11-mer RNAs (50 μM). For each condition, the formation of droplets was analyzed by fluorescence microscopy. The scale bar represents 10 μm. IB, inclusion body.

11-mer RNA with 5′ OH were observed in the presence of 11-mer RNAs with 5′ ppp and ^{7m}Gppp (Fig. 7*D*).

Altogether, our data revealed that coincubation of P with monomeric N does not allow pseudo-IBs morphogenesis *in vitro*, and that the addition of short RNAs is not sufficient to induce phase separation. Overall, these results showed that N oligomerization in the presence of RNA is critical for the morphogenesis of pseudo-IBs.

Discussion

Like for the majority of viruses belonging to the *Mononegavirales* order, HRSV replication and transcription take place within cytoplasmic viral factories called IBs that concentrate the viral and cellular proteins required for these activities, as well as neosynthesized antigenomic and genomic RNAs and viral mRNAs. Replication leads to the synthesis and amplification of full-length negative-sense genomic and positive sense antigenomic RNAs, which are encapsidated by N in its RNA-free form N^0, forming the so-called NCs, in contrast to viral mRNAs. This specificity of encapsidation of viral genomes and antigenomes by N remains unexplained. Given the strong tendency of N^0 to oligomerize on RNAs, some particular mechanisms might regulate the specificity of viral RNA encapsidation and thus the transition from N^0 to N-RNA. The aim of this work was to investigate whether specificity of encapsidation could be explained either by the sequence or the nature of the 5′ end of RNAs. Here, using a chimeric protein

composed of full-length N and P40, a peptide corresponding to the 40 N-terminal residues of P, we showed that this construct is competent for RNA encapsidation *in vitro*, even in the presence of full-length P protein. This first observation shows that P is not sufficient to prevent RNA encapsidation by N, suggesting the existence of another factor that could regulate the transition from monomeric N^0 to N-RNA assembly in infected cells, most likely by enhancing the stability of N^0. In agreement with a recent publication by Gao *et al.* (47), our results also confirmed that RNA as short as 7-mer can be encapsidated, and that N oligomerization on RNAs always leads to the formation of N-RNA rings *in vitro*. We showed that the minimum length for stable encapsidation was 11 nucleotides, revealing that RNA length is critical for the stability of N-RNA oligomers. However, we cannot exclude that the presence of P40 fused to the C-terminus of N may partially alter N oligomerization. In contrast to measles virus for which helical NC can form *in vitro* using recombinant N protein and 6-mer RNAs (4), our data suggest that additional factors such as viral or cellular partners or posttranslational modifications maybe required for proper HRSV N oligomerization along RNA to obtain helical NCs.

Currently, the specificity of encapsidation of viral genomic and antigenomic RNAs by N is unknown. The difference between the 5′ ends of mRNAs (capped) and genomic and antigenomic RNAs (ppp) could explain this mechanism. However, we found that the presence of either ppp or ^{7m}Gppp at the 5′ end instead of OH only partially impedes the ability of N to encapsidate RNAs, most probably by creating steric hindrance. In light of the recent discovery of subcompartments called IBs-associated granules within IBs, that specifically concentrate M2-1 and viral mRNA (8), we hypothesize that the exclusion of viral mRNA complexed to M2-1 from the polymerase complex could contribute, at least in part, to the segregation of mRNAs and thereby specificity of genome encapsidation by N. Our study highlighted the absence of encapsidation of short 5′ ppp RNAs. This observation suggests that the 5′ ppp end of genomes and antigenomes should be exposed and detected by sensors of the cellular innate immune system such as RIG-I. Recently, cryo-EM studies of Newcastle disease virus, Sendaï, Nipah, and cetacean morbillivirus have revealed heterogeneity in NC assembly, with the presence of double-headed helical structures (53–56). Such an assembly could hide the 5′ end of antigenomes and genomes, thus preventing 5′ ppp detection by cellular sensors. However, further investigation will be needed to decipher the accessibility and protection of the 5′ end of viral genomes.

Finally, we investigated the importance of P, N oligomerization, and RNAs in the morphogenesis of pseudo-IBs *in vitro*. The tetrameric RSV P protein has intrinsically disordered regions involved in multiple transient interactions known to be critical for phase separation and is a major scaffolding component of IBs (39). When P was mixed with a monomeric N^0-like protein (N-P40) and RNAs are too short to be encapsidated, no phase separation was observed, indicating that the presence of RNA-N oligomers is critical for pseudo-IBs formation. Interestingly, the length of encapsidated RNAs seems to modulate the size of pseudo-IBs. These observations correlate with the fact that RNAs have been shown to play a major role in liquid-liquid phase separation mechanisms (49, 50). Further characterization of IBs morphogenesis in the presence of RSV helical NC should be of great interest, as the size and high flexibility of these structures could modulate IBs morphogenesis. A recent cryo-electron tomography study of RSV-infected cells has revealed the presence of N rings in filamentous RSV particles (57), showing for the first time the heterogeneity of N assembly in the cell. The role of these structures during viral cycle, that is, IBs morphogenesis, control of the innate immune response to infection, and virion assembly remains to be determined.

Experimental procedures

Plasmid constructs

The gene sequence of the nucleoprotein N was amplified without stop codon by PCR using Pfu DNA polymerase (Stratagene) and cloned in the pET28a+ vector, at BamHI and XhoI sites. The oligonucleotides used were as follows: 5′-GCCGCCGGATCCATGGCTCTTAGAAAG TCAAG TTG-3′ (BamHI) and 5′-GAGGAGCTCGAGAAG CTCTA-CATCATTATCTTTTGG-3′ (XhoI). The sequence-coding TEV cleavage site was then introduced at the BamHI site after annealing of the oligonucleotides 5′-GATCCGAGAACCT ATATTTCCAGG-3′ and 5′-GATCCCTGGAAATATAGG TTCTCG-3’. Finally, the sequence coding for the 40 N-terminal residues of P was PCR amplified using the oligonucleotides 5′-GAGGAGCTCGAGGGTAGCGGTAGCGGTAG CGGTAGCATGGAAAAGTTTGC TCCTGAATTCC-3′ (containing the sequence coding for 4 Gly/Ser, underlined) and 5′-GAG GAGCTCGAGTTAGATACTATCTTTTTT CTTCCCATC-3′ (with a stop codon at the 3′ end, underlined) and inserted at the XhoI site. The viral sequences derived from the human RSV strain ATCC VR-26 (GenBank accession number: AY911262.1). The final plasmid allows the expression of the fusion protein 6xHis-N-4xgs-P40 containing a TEV cleavage site upstream of the N sequence. For expression and purification of recombinant mCherry-N, N, and P-BFP proteins, the previously described pET-mCherry-N, pET-N, and pET-P-BFP plasmids were used (37, 39).

Expression and purification of the recombinant proteins

The *E. coli* BL21 (DE3) bacteria strain (Novagen) were transformed by the pET-N-P40 plasmid. Cultures were grown at 37 °C in 2xYT medium containing 50 μg/ml kanamycin. After 8 h, an equal volume of 2xYT medium containing 50 μg/ml kanamycin was added to the cultures, and protein expression was induced by the addition of 80 μg/ml IPTG overnight at 28 °C. Bacteria were then harvested by centrifugation. Pellets were resuspended in lysis buffer (20 mM Tris–HCl, pH 8, 500 mM NaCl, 0.1% Triton X-100, 10 mM imidazole, 4 mM benzamidine, 1 mg/ml lysozyme, and complete protease inhibitor cocktail (Roche)). After incubation on

ice for 30 min, the lysates were sonicated, benzonase (Novagen) (final concentration 5 U/ml) and RNase A (final concentration of 1 U/ml) were added to the lysate, followed by incubation for 30 min at room temperature, finally NaCl was added (up to a concentration of 1 M). After centrifugation at 10,000 *g* for 30 min at 4 °C, the lysates were incubated with chelating Sepharose Fast Flow beads (GE Healthcare) charged with Ni^{2+}, for 1 h at 4 °C. Beads were washed with washing buffers (20 mM Tris–HCl, pH 8, 1 M NaCl, 4 mM benzamidine) with increasing imidazole concentrations (10, 50, and 100 mM), before elution of the protein using 600 mM imidazole. Purified proteins were then loaded on a Hi-Load 16/600 Superdex 200 column (GE Healthcare) and eluted in 20 mM Tris–HCl, pH 8.5, 1 M NaCl. Then, the purified protein was dialyzed against 10 mM Tris–HCl, pH 8.5, with decreasing NaCl concentrations (500 and 300 mM) buffers, for 4 h at each step, at 4 °C. Finally, the purified protein was concentrated using a centrifugal concentrator with a MWCO of 10 kDa (vivaspin turbo 4, Sartorius). WT mCherry-N, N, and P-BFP proteins were expressed and purified as previously described (39).

Synthesis of RNA substrates

RNA sequences were chemically synthesized on a solid support using an ABI 394 automated synthesizer with 2′-*O*-pivaloyloxymethyl 3′-*O*-phosphoramidite ribonucleosides and with 2′-*O*-methyl 3′-*O*-phosphoramidite adenosine to obtain $^{7m}GpppA_m$-RNA (ChemGenes Corp.) (58). After RNA assembly, depending on the desired 5′ end of the RNA, 3 different processes were applied. For 5′ OH-RNA sequences, the solid support was directly subjected to a basic treatment (28% aqueous ammonia solution at r.t for 3 h) to recover the crude RNA material. In the other 2 cases, the 5′-hydroxyl group was phosphorylated and the resulting *H*-phosphonate derivative was oxidized and activated to a phosphoroimidazolidate derivative to react with pyrophosphate or GDP, yielding ppp-RNA (59) or Gppp-RNA (60), respectively. After deprotection and release from the solid support by the same ammonia treatment as for 5′-OH RNA, all RNA substrates were purified by IEX-HPLC (>95% pure) and their identity was confirmed by MALDI-TOF spectrometry. *N*7-methylation of the cap structure (Gppp) was performed using human (guanine-*N*7)-MTase to obtain ^{7m}Gppp-RNA (60).

RNA–N-P40 complexes formation

RNA oligonucleotides (15 μM) and purified N-P40 protein (10 μM) in 20 mM Tris–HCl, pH 8.5, 300 mM NaCl buffer were coincubated for 30 min at room temperature. The presence of RNA was assessed by measuring the A_{260nm}/A_{280nm} absorption ratio. For RNase treatment, samples were incubated overnight at 4 °C in the presence of RNase A (PureLink, Invitrogen), then dialyzed against 10 mM NaP, 300 mM NaF, pH 8.5, for 3 h at 4 °C. After dialysis, the A_{260nm}/A_{280nm} absorption ratio was measured.

Band shift on native polyacrylamide and agarose gels

50% sucrose loading buffer was added to the samples before loading either on native 4% native polyacrylamide gel or on native 1% agarose gel. For polyacrylamide native gel analysis, migration was performed in 0.2 × TBE (pH 8.0 for 2 h at 200 V at 4 °C), and gels were stained with Coomassie blue. For agarose native gel analysis, migration was performed in 1× Tris–Glycine buffer during 1 h 30 at 80 V before staining with amido black 10B.

Dynamic light scattering

Size measurement of purified N-P40 alone or incubated with RNAs was performed at 20 °C using a helium-neon laser wavelength of 633 nm and detection angle of 173° with a Zetasizer Nano (Malvern). Ten measurements were made, with an acquisition time of 10 s for each measurement. Hydrodynamic diameters were calculated using the Zetasizer software provided by the instrument manufacturer (https://www.malvernpanalytical.com/fr/support/product-support/software/Zetasizer-Nano-software-update-v3-30). The results were presented as size distribution (nm).

CD spectroscopy

CD experiments were performed on a J-810 spectropolarimeter (Jasco) in a thermostated cell holder at 20 °C. Spectra of N-P40 and RNA–N-P40 complexes were measured after dialysis against 10 mM NaP, 300 mM NaF, pH 8.5 buffer, and at concentrations of 10 μM. Far-UV spectra (190–260 nm) were recorded in a 0.5 mm path-length quartz cell using a bandwidth of 2 nm and an integration time of 1 s. Near-UV spectra (260–320 nm) were recorded in a 10 mm path-length quartz cell using a bandwidth of 2 nm and an integration time of 1 s. Each spectrum was the average of 3 scans, with a scan rate of 100 nm/min and 50 nm/min for far-UV and near-UV spectra, respectively. Correction by subtracting the signal from the buffer was made and the spectra were smoothed with the fast Fourier transform filter (Jasco Software), and data were treated as previously described (37).

Negative stain electron microscopy observations of N-P40–RNA complexes

Three microliters of sample were applied to the clean side of carbon on a carbon–mica interface and stained with 2% sodium silicotungstate. Micrographs were recorded on a Thermofisher Scientific Tecnai T12 microscope operated at 120 kV with a Gatan Orius 1000 camera. Images were recorded at a nominal magnification of 23000× resulting in a pixel size of 2.8 Å.

In vitro *assay of pseudo-IBs formation*

As previously described (39), mCherry-N and P proteins or P-BFP and WT N or N-P40 recombinant proteins alone or in the presence of RNAs in 20 mM Tris–HCl pH 8.5, 150 mM NaCl buffer were coincubated at different P/N molecular ratio on glass slides, and the molecular-crowding agent Ficoll was

added on the droplets of solution. Then, coverslips were laid on the droplets. For RNase treatment, N-P40 recombinant protein was preincubated in the presence of 8-mer and 11-mer RNAs, then incubated half an hour at room temperature in the presence of RNase A (PureLink, Invitrogen). Pseudo-IBs were then observed with a Nikon TE200 inverted microscope equipped with a Photometrics CoolSNAP ES2 camera. Images were processed using MetaVue software (Molecular Devices, https://www.nikonusa.com/fileuploads/pdfs/MetaVue.pdf) and ImageJ software (https://imagej.nih.gov/ij/index.html).

Data availability

All data are contained within the article.

Acknowledgments—We thank Stephane Duquerroy (Institut Pasteur, France) for the scientific discussions related to this work. Protein purification benefited from the purchase of a gel filtration system funded by the Région Ile de France, France (DIM OneHealth 2018). For electron microscopy observations, this work used the EM platform of the Grenoble Instruct-ERIC center (ISBG; UAR 3518 CNRS-CEA-UGA-EMBL) within the Grenoble Partnership for Structural Biology (PSB), supported by the French Agence Nationale de la Recherche (ANR-10-INBS-0005-02) and financed within the University Grenoble Alpes graduate school, France and the specific program ANR-17-EURE-0003. The electron microscope facility is supported by the Auvergne-Rhône-Alpes Region, the Fondation Recherche Médicale (FRM), the fonds FEDER, and the GIS-Infrastructures en Biologie Santé et Agronomie (IBISA). This work was carried out with the financial support of the French Agence Nationale de la Recherche, France, specific programs ANR DecRisP n° ANR-19-CE11-0017 and ANR RSVFact n° ANR-21-CE15-0030-02.

Author contributions—L. G., J.-F. E., and M. G. methodology; L. G., C.-A. R., I. G., D. C., J. T., J.-J. V., and F. D. investigation; M. G. writing–original draft; J.-F. E. and M. G. writing–review and editing.

Conflict of interest—The authors declare that they have no conflicts of interest with the contents of this article.

Abbreviations—The abbreviations used are: DLS, dynamic light scattering; HMPV, human metapneumovirus; HRSV, human respiratory syncytial virus; IB, inclusion body; NC, nucleocapsid; ns-EM, negative stain electron microscopy.

References

1. Rima, B., Collins, P., Easton, A., Fouchier, R., Kurath, G., Lamb, R. A., *et al.* (2018) Problems of classification in the family Paramyxoviridae. *Arch. Virol.* **163**, 1395–1404
2. Collins, P. L., and Crowe, J. E. (2007) Respiratory syncytial virus and metapneumovirus. In: Knipe, D. M., Howley, P. M., eds. *Fields Virology*, 5th Ed., Lippincott Williams & Wilkins, Philadelphia: 1601–1646
3. Fearns, R., and Plemper, R. K. (2017) Polymerases of paramyxoviruses and pneumoviruses. *Virus Res.* **234**, 87–102
4. Guseva, S., Milles, S., Jensen, M. R., Salvi, N., Kleman, J. P., Maurin, D., *et al.* (2020) Measles virus nucleo- and phosphoproteins form liquid-like phase-separated compartments that promote nucleocapsid assembly. *Sci. Adv.* **6**, eaaz7095
5. Heinrich, B. S., Maliga, Z., Stein, D. A., Hyman, A. A., and Whelan, S. P. J. (2018) Phase transitions drive the formation of vesicular stomatitis virus replication compartments. *mBio* **9**. e02290-17
6. Nikolic, J., Le Bars, R., Lama, Z., Scrima, N., Lagaudriere-Gesbert, C., Gaudin, Y., *et al.* (2017) Negri bodies are viral factories with properties of liquid organelles. *Nat. Commun.* **8**, 58
7. Zhou, Y., Su, J. M., Samuel, C. E., and Ma, D. (2019) Measles virus forms inclusion bodies with properties of liquid organelles. *J. Virol.* **93**. e00948-19
8. Rincheval, V., Lelek, M., Gault, E., Bouillier, C., Sitterlin, D., Blouquit-Laye, S., *et al.* (2017) Functional organization of cytoplasmic inclusion bodies in cells infected by respiratory syncytial virus. *Nat. Commun.* **8**, 563
9. Afonso, C. L., Amarasinghe, G. K., Banyai, K., Bao, Y., Basler, C. F., Bavari, S., *et al.* (2016) Taxonomy of the order Mononegavirales: update 2016. *Arch. Virol.* **161**, 2351–2360
10. Rima, B., Collins, P., Easton, A., Fouchier, R., Kurath, G., Lamb, R. A., *et al.* (2017) ICTV virus taxonomy profile: pneumoviridae. *J. Gen. Virol.* **98**, 2912–2913
11. Shi, T., McAllister, D. A., O'Brien, K. L., Simoes, E. A. F., Madhi, S. A., Gessner, B. D., *et al.* (2017) Global, regional, and national disease burden estimates of acute lower respiratory infections due to respiratory syncytial virus in young children in 2015: a systematic review and modelling study. *Lancet* **390**, 946–958
12. Nair, H., Nokes, D. J., Gessner, B. D., Dherani, M., Madhi, S. A., Singleton, R. J., *et al.* (2010) Global burden of acute lower respiratory infections due to respiratory syncytial virus in young children: a systematic review and meta-analysis. *Lancet* **375**, 1545–1555
13. Pneumonia Etiology Research for Child Health Study Group (2019) Causes of severe pneumonia requiring hospital admission in children without HIV infection from Africa and Asia: the PERCH multi-country case-control study. *Lancet* **394**, 757–779
14. Falsey, A. R., Hennessey, P. A., Formica, M. A., Cox, C., and Walsh, E. E. (2005) Respiratory syncytial virus infection in elderly and high-risk adults. *N. Engl. J. Med.* **352**, 1749–1759
15. Asner, S., Stephens, D., Pedulla, P., Richardson, S. E., Robinson, J., and Allen, U. (2013) Risk factors and outcomes for respiratory syncytial virus-related infections in immunocompromised children. *Pediatr. Infect. Dis. J.* **32**, 1073–1076
16. Shah, J. N., and Chemaly, R. F. (2011) Management of RSV infections in adult recipients of hematopoietic stem cell transplantation. *Blood* **117**, 2755–2763
17. Collins, P. L., and Melero, J. A. (2011) Progress in understanding and controlling respiratory syncytial virus: still crazy after all these years. *Virus Res.* **162**, 80–99
18. Collins, P. L., Hill, M. G., Camargo, E., Grosfeld, H., Chanock, R. M., and Murphy, B. R. (1995) Production of infectious human respiratory syncytial virus from cloned cDNA confirms an essential role for the transcription elongation factor from the 5' proximal open reading frame of the M2 mRNA in gene expression and provides a capability for vaccine development. *Proc. Natl. Acad. Sci. U.S.A.* **92**, 11563–11567
19. Fearns, R., and Collins, P. L. (1999) Role of the M2-1 transcription antitermination protein of respiratory syncytial virus in sequential transcription. *J. Virol.* **73**, 5852–5864
20. Noton, S. L., and Fearns, R. (2015) Initiation and regulation of paramyxovirus transcription and replication. *Virology* **479-480**, 545–554
21. Noton, S. L., Tremaglio, C. Z., and Fearns, R. (2019) Killing two birds with one stone: how the respiratory syncytial virus polymerase initiates transcription and replication. *PLoS Pathog.* **15**, e1007548
22. Hefti, E., and Bishop, D. H. (1975) The 5' nucleotide sequence of vesicular stomatitis viral RNA. *J. Virol.* **15**, 90–96
23. Hefti, E., and Bishop, D. H. (1975) The 5' sequence of VSV viral RNA and its *in vitro* transcription product RNA. *Biochem. Biophys. Res. Commun.* **66**, 785–792
24. Bakker, S. E., Duquerroy, S., Galloux, M., Loney, C., Conner, E., Eleouet, J. F., *et al.* (2013) The respiratory syncytial virus nucleoprotein-RNA complex forms a left-handed helical nucleocapsid. *J. Gen. Virol.* **94**, 1734–1738

25. Samal, S. K., and Collins, P. L. (1996) RNA replication by a respiratory syncytial virus RNA analog does not obey the rule of six and retains a nonviral trinucleotide extension at the leader end. *J. Virol.* **70**, 5075–5082
26. Cowton, V. M., McGivern, D. R., and Fearns, R. (2006) Unravelling the complexities of respiratory syncytial virus RNA synthesis. *J. Gen. Virol.* **87**, 1805–1821
27. Tawar, R. G., Duquerroy, S., Vonrhein, C., Varela, P. F., Damier-Piolle, L., Castagne, N., *et al.* (2009) Crystal structure of a nucleocapsid-like nucleoprotein-RNA complex of respiratory syncytial virus. *Science* **326**, 1279–1283
28. Leyrat, C., Yabukarski, F., Tarbouriech, N., Ribeiro, E. A., Jr., Jensen, M. R., Blackledge, M., *et al.* (2011) Structure of the vesicular stomatitis virus N(0)-P complex. *Plos Pathog.* **7**, e1002248
29. Yabukarski, F., Lawrence, P., Tarbouriech, N., Bourhis, J. M., Delaforge, E., Jensen, M. R., *et al.* (2014) Structure of Nipah virus unassembled nucleoprotein in complex with its viral chaperone. *Nat. Struct. Mol. Biol.* **21**, 754–759
30. Esneau, C., Raynal, B., Roblin, P., Brule, S., Richard, C. A., Fix, J., *et al.* (2019) Biochemical characterization of the respiratory syncytial virus N(0)-P complex in solution. *J. Biol. Chem.* **294**, 3647–3660
31. Renner, M., Bertinelli, M., Leyrat, C., Paesen, G. C., Saraiva de Oliveira, L. F., Huiskonen, J. T., *et al.* (2016) Nucleocapsid assembly in pneumoviruses is regulated by conformational switching of the N protein. *eLife* **5**, e12627
32. Aggarwal, M., Leser, G. P., Kors, C. A., and Lamb, R. A. (2018) Structure of the paramyxovirus parainfluenza virus 5 nucleoprotein in complex with an amino-terminal peptide of the phosphoprotein. *J. Virol.* **92**, e01304–e01317
33. Zhu, T., Song, H., Peng, R., Shi, Y., Qi, J., and Gao, G. F. (2017) Crystal structure of the Marburg virus nucleoprotein core domain chaperoned by a VP35 peptide reveals a conserved drug target for Filovirus. *J. Virol.* **91**. e00996-17
34. Guryanov, S. G., Liljeroos, L., Kasaragod, P., Kajander, T., and Butcher, S. J. (2015) Crystal structure of the measles virus nucleoprotein core in complex with an N-terminal region of phosphoprotein. *J. Virol.* **90**, 2849–2857
35. Kirchdoerfer, R. N., Abelson, D. M., Li, S., Wood, M. R., and Saphire, E. O. (2015) Assembly of the Ebola virus nucleoprotein from a chaperoned VP35 complex. *Cell Rep.* **12**, 140–149
36. Dong, X., Wang, X., Xie, M., Wu, W., and Chen, Z. (2022) Structural basis of human parainfluenza virus 3 unassembled nucleoprotein in complex with its viral chaperone. *J. Virol.* **96**, e0164821
37. Galloux, M., Gabiane, G., Sourimant, J., Richard, C. A., England, P., Moudjou, M., *et al.* (2015) Identification and characterization of the binding site of the respiratory syncytial virus phosphoprotein to RNA-free nucleoprotein. *J. Virol.* **89**, 3484–3496
38. Garcia, J., Garcia-Barreno, B., Vivo, A., and Melero, J. A. (1993) Cytoplasmic inclusions of respiratory syncytial virus-infected cells: Formation of inclusion bodies in transfected cells that coexpress the nucleoprotein, the phosphoprotein, and the 22K protein. *Virology* **195**, 243–247
39. Galloux, M., Risso-Ballester, J., Richard, C. A., Fix, J., Rameix-Welti, M. A., and Eleouet, J. F. (2020) Minimal elements required for the formation of respiratory syncytial virus cytoplasmic inclusion bodies in vivo and in vitro. *mBio* **11**, e01202–e01220
40. Risso-Ballester, J., Galloux, M., Cao, J., Le Goffic, R., Hontonnou, F., Jobart-Malfait, A., *et al.* (2021) A condensate-hardening drug blocks RSV replication *in vivo*. *Nature* **595**, 596–599
41. Richard, C. A., Rincheval, V., Lassoued, S., Fix, J., Cardone, C., Esneau, C., *et al.* (2018) RSV hijacks cellular protein phosphatase 1 to regulate M2-1 phosphorylation and viral transcription. *PLoS Pathog.* **14**, e1006920
42. Bajorek, M., Galloux, M., Richard, C. A., Szekely, O., Rosenzweig, R., Sizun, C., *et al.* (2021) Tetramerization of phosphoprotein is essential for respiratory syncytial virus budding while its N terminal region mediates direct interactions with the matrix protein. *J. Virol.* **11**, 1225
43. Sourimant, J., Rameix-Welti, M. A., Gaillard, A. L., Chevret, D., Galloux, M., Gault, E., *et al.* (2015) Fine mapping and characterization of the L-polymerase-binding domain of the respiratory syncytial virus phosphoprotein. *J. Virol.* **89**, 4421–4433
44. Gilman, M. S. A., Liu, C., Fung, A., Behera, I., Jordan, P., Rigaux, P., *et al.* (2019) Structure of the respiratory syncytial virus polymerase complex. *Cell* **179**, 193–204.e14
45. Tran, T. L., Castagne, N., Bhella, D., Varela, P. F., Bernard, J., Chilmonczyk, S., *et al.* (2007) The nine C-terminal amino acids of the respiratory syncytial virus protein P are necessary and sufficient for binding to ribonucleoprotein complexes in which six ribonucleotides are contacted per N protein protomer. *J. Gen. Virol.* **88**, 196–206
46. Galloux, M., Tarus, B., Blazevic, I., Fix, J., Duquerroy, S., and Eleouet, J. F. (2012) Characterization of a viral phosphoprotein binding site on the surface of the respiratory syncytial nucleoprotein. *J. Virol.* **86**, 8375–8387
47. Gao, Y., Cao, D., Ahn, H. M., Swain, A., Hill, S., Ogilvie, C., *et al.* (2020) *In vitro* trackable assembly of RNA-specific nucleocapsids of the respiratory syncytial virus. *J. Biol. Chem.* **295**, 883–895
48. Banani, S. F., Lee, H. O., Hyman, A. A., and Rosen, M. K. (2017) Biomolecular condensates: organizers of cellular biochemistry. *Nat. Rev. Mol. Cell. Biol.* **18**, 285–298
49. Alberti, S., Gladfelter, A., and Mittag, T. (2019) Considerations and challenges in studying liquid-liquid phase separation and biomolecular condensates. *Cell* **176**, 419–434
50. Alberti, S., Saha, S., Woodruff, J. B., Franzmann, T. M., Wang, J., and Hyman, A. A. (2018) A user's guide for phase separation assays with purified proteins. *J. Mol. Biol.* **430**, 4806–4820
51. Shimobayashi, S. F., Ronceray, P., Sanders, D. W., Haataja, M. P., and Brangwynne, C. P. (2021) Nucleation landscape of biomolecular condensates. *Nature* **599**, 503–506
52. Brocca, S., Grandori, R., Longhi, S., and Uversky, V. (2020) Liquid-liquid phase separation by intrinsically disordered protein regions of viruses: roles in viral life cycle and control of virus-host interactions. *Int. J. Mol. Sci.* **21**, 9045
53. Song, X., Shan, H., Zhu, Y., Hu, S., Xue, L., Chen, Y., *et al.* (2019) Self-capping of nucleoprotein filaments protects the Newcastle disease virus genome. *Elife* **8**, e45057
54. Zhang, N., Shan, H., Liu, M., Li, T., Luo, R., Yang, L., *et al.* (2021) Structure and assembly of double-headed Sendai virus nucleocapsids. *Commun. Biol.* **4**, 494
55. Ker, D. S., Jenkins, H. T., Greive, S. J., and Antson, A. A. (2021) CryoEM structure of the Nipah virus nucleocapsid assembly. *Plos Pathog.* **17**, e1009740
56. Zinzula, L., Beck, F., Klumpe, S., Bohn, S., Pfeifer, G., Bollschweiler, D., *et al.* (2021) Cryo-EM structure of the cetacean morbillivirus nucleoprotein-RNA complex. *J. Struct. Biol.* **213**, 107750
57. Conley, M. J., Short, J. M., Burns, A. M., Streetley, J., Hutchings, J., Bakker, S. E., *et al.* (2022) Helical ordering of envelope-associated proteins and glycoproteins in respiratory syncytial virus. *EMBO J.* **41**, e109728
58. Parey, N., Baraguey, C., Vasseur, J. J., and Debart, F. (2006) First evaluation of acyloxymethyl or acylthiomethyl groups as biolabile 2'-O-protections of RNA. *Org. Lett.* **8**, 3869–3872
59. Zlatev, I., Lavergne, T., Debart, F., Vasseur, J. J., Manoharan, M., and Morvan, F. (2010) Efficient solid-phase chemical synthesis of 5'-triphosphates of DNA, RNA, and their analogues. *Org. Lett.* **12**, 2190–2193
60. Thillier, Y., Decroly, E., Morvan, F., Canard, B., Vasseur, J. J., and Debart, F. (2012) Synthesis of 5' cap-0 and cap-1 RNAs using solid-phase chemistry coupled with enzymatic methylation by human (guanine-N(7))-methyl transferase. *RNA* **18**, 856–868